

Authors Version

Lars Steinberg, Ravisankar Naraparaju, Mirko Heckert, Christoph Mikulla, Uwe Schulz, Christoph Leyens

Erosion behavior of EB-PVD 7YSZ coatings under corrosion/erosion regime: Effect of TBC microstructure and the CMAS chemistry

Journal of the European Ceramic Society 38 (15) 2018

Available online <https://doi.org/10.1016/j.jeurceramsoc.2018.06.039>

Erosion behavior of EB-PVD 7YSZ coatings under corrosion/erosion regime: Effect of TBC microstructure and the CMAS chemistry

Lars Steinberg¹⁾, Ravisankar Naraparaju²⁾, Mirko Heckert¹⁾, Christoph Mikulla²⁾, Uwe Schulz²⁾, Christoph Leyens¹⁾

1) TU Dresden, Institute of Materials Science (IfWW), D-01062 Dresden (Germany)

2) German Aerospace Center (DLR), Institute of Materials Research, D-51170 Cologne (Germany)

Declarations of interest: none

Corresponding author: Lars Steinberg

Email address: Lars.Steinberg@tu-dresden.de

Phone: 0049 351 46342320

Fax: 0049 351 46342482

Abstract

Aero-engines operating in dust-laden environments often encounter a lot of dust/sand that causes a severe problem to the TBCs by means of erosion. As the turbine entry temperatures are rising, molten sand is also a big concern to the life-time of TBCs.

This paper deals with the TBC behavior under the combined influence of erosion and corrosion attack. Variations in TBC morphology, CMAS infiltration time and CMAS composition and their influence on the erosion resistance at room temperature were investigated. Two different EB-PVD 7YSZ morphologies consisting of a different porosity arrangement were tested in the erosion/corrosion regime. The more 'Feathery' structure has a better resistance to erosion compared to a more columnar 'Normal' structure, which leads to less degradation of the TBC. However, under the influence of CMAS infiltration the effect was found to be reversed. In general, CMAS-infiltrated EB-PVD TBCs exhibit a higher erosion resistance than the non-infiltrated one's.

Keywords: TBC; Erosion; CMAS; EB-PVD; 7YSZ

1. Introduction

The increased performance of gas turbines leads to a more efficient mode of operation [1]. The development of thermal barrier coatings (TBC) enable the turbines to run at higher temperature by protecting components of the engine like the combustor or turbine blades and vanes against overheating [2]. Several intrinsic and extrinsic mechanisms exist that contribute to the damage of TBCs [3]. During the ground idle as well as the descent flight situation, small particles of ingested sand can generate erosive wear damage on TBCs at low temperature [4]. At higher operating temperatures during cruise in the troposphere, dust particles and volcanic ashes can be ingested into the engine and deposit on the TBC. Since the operation temperature exceeds the melting point of volcanic ashes (>1150 °C) and sand (>1230 °C), the degradation of TBCs by molten deposits comes into focus [5,6].

CaO-MgO-SiO₂-Al₂O₃ (CMAS) and volcanic ash (VA) which stick to the hot surface of the turbine blades can melt and infiltrate the TBCs at these temperatures [1,7,8]. The infiltrated CMAS leads to a dissolution of the t'-phase and a re-precipitation of monoclinic and cubic YSZ during cooling [5]. The monoclinic phase transformation causes a volume expansion, which leads to stresses in the TBC and may result in delamination of the coating. Furthermore, the infiltrated and solidified CMAS increases the Young's modulus and lowers the strain tolerance of the electron beam physical vapor deposition (EB-PVD)-TBC. The mismatch between the thermal expansion coefficients of the CMAS-infiltrated TBC in comparison to the bond-coat/Ni-base superalloy generates thermal stresses and may result in delamination, too [9,10].

Ghini et al. [11] have discussed the global distribution of CMAS depending on different parameters like wind and the soil erosion tendency. Based on this field of research airplanes could take routes, which have a minor contamination of sand or volcanic ashes. Since in many cases it is not possible to avoid areas with high CMAS loads, it is necessary to improve the CMAS- and erosion resistance of TBCs.

Considerable amount of research has been done in the field of erosion behavior of TBCs at room temperature as well as high temperature by Wellman et al. [9,12–15] and other scientific groups [16–23]. The effect of CMAS on the mechanical and chemical degradation of the TBCs was thoroughly studied [1,10,24,25]. However, very few attempts have been made on understanding the combined impact of erosion and CMAS effects [16,26]. Wellman and Nicholls [26] found that fully CMAS-infiltrated EB-PVD TBCs behave like a continuum during erosion and slightly improve erosion behavior under room temperature compared to pure TBC. Cracks propagate near the surface through several columns connected by CMAS infiltration before TBC material removal occurs. Rezanka et al. [19] discussed the influence of different TBC microstructures produced by PS-PVD, EB-PVD and APS on

CMAS corrosion resistance as well as erosion behavior. Nevertheless, the combined impact of both erosion and CMAS effects was not considered.

The present study is focused on three main issues: (i) the erosion behavior of the as-coated TBC with two different microstructures ('Feathery' and 'Normal'), (ii) the erosion mechanisms concerning CMAS-infiltrated TBCs, since both damage mechanisms (erosion/corrosion) occur parallelly and competitively in a turbine, and (iii) the influence of CMAS chemistry on the erosion behavior of fully infiltrated TBCs with varying morphology. A better understanding of the impact of changes in TBC-morphology, degradation level of the TBC depending on the duration of CMAS infiltration, as well as CMAS composition on erosion guides development strategies for new CMAS-resistant TBCs.

2. Experimental procedure

2.1. Sample preparation

EB-PVD yttria stabilized zirconia (7YSZ) coatings with two different morphologies namely 'Feathery' and 'Normal' were produced at the DLR. The coating parameters were published elsewhere [27,28]. TBC thickness was around 400 μm . Al_2O_3 sheets with a size of (34x20x1) mm^3 were used as substrate material. The 'Feathery' as well as the 'Normal' structures were produced in two different batches. In order to precisely describe the numerous experiments with two different chemical compositions of CMAS and one Iceland volcanic ash (Iceland VA) on two different TBC microstructures for different infiltration times, a particular nomenclature is used depending on the type of infiltration history that is presented in Table 2. The corresponding nomenclature of samples consists of abbreviations of morphology (F for 'Feathery', N for 'Normal')/ type of CMAS (C1 for CMAS 1, C2 for CMAS 2 and I for Iceland VA)/ duration of heat treatment (5 for 5 min., 8 for 8 min. and 300 for 300 min). The influence of CMAS 2 was only investigated in combination with the 'Normal' microstructure. Non-infiltrated 'Feathery' samples are marked as F/-/- and 'Normal' as N/-/-.

Due to the variation of CMAS composition around the globe and the well-studied effect of CMAS chemistry on the reaction mechanism two different synthesized compositions (CMAS 1/-2) as well as one real Iceland VA were used in the experiments. The chemical compositions of the used CMAS/Iceland VA are presented in Table 1. They varied in their SiO_2 content which influenced the viscosity and had a high impact on the infiltration behavior. Furthermore, the different morphologies of CMAS (crystalline) and Iceland VA (amorphous) also effected the mechanical properties of the infiltrated TBCs. The melting points and their viscosities of the deposits that were evaluated previously [6,29,30] are included in the table, too. CMAS/Iceland VA paste in the amounts of 10 mg/cm^2 was applied on the coatings and the infiltration tests were conducted at 1250 $^\circ\text{C}$ for different times (5 min or 8 min for the short-term and 300 min for the long-term infiltration). While the long-term infiltration leads to an entire infiltration as well as a phase transformation (described in 3.4) which might change the mechanical properties of the TBC, the short-term infiltration guarantees only an entire infiltration without causing much damage to the phase stability of the coating. The different durations of short-term infiltration were needed since the 'Feathery' structure retards the CMAS infiltration [27] compared to the 'Normal' structure [29]. Consequently, F/C1/8 was not fully infiltrated before 8 min at 1250 $^\circ\text{C}$ while 'Normal' was fully infiltrated already after 5 min. The short-term infiltrated samples were removed from the hot furnace directly after the defined infiltration time. This procedure guarantees a rapid cooling. The long-term infiltrated samples obtained a controlled cooling of 10 K/min.

Table 1 Summary of CMAS and Iceland VA compositions in mol.%, main phases, viscosity and melting temperature [6,29,30].

Mol.%	Ca O	Mg O	Al_2O_3	SiO_2	Fe O	TiO_2	Na_2 O	K_2 O	Main phases	Viscosity at 1250 $^\circ\text{C}$ Log Pa.s	Melting point $^\circ\text{C}$
CMAS 1 = C1	24. 7	12.4	11.1	41. 7	8.7	1.6	-	-	Pyrox- ene+Anorthite	-0.25	1230- 1250

CMAS 2 = C2	32.4	11,2	9.8	37.3	7.82	1.4	-	-	Pyroxene+Melilite	-0.69	1215-1245
Ice-land VA = I	12.5	6.1	7.4	49.7	17.6	4.3	2	0.4	Amorphous	3.5	1150

Table 2 Tested 7YSZ EB-PVD samples with variations in morphology, CMAS compositions and heat treatment.

Sample designation	Morphology	Type of CMAS	Duration of heat treatment [min]
F/-/-	'Feathery'	-	-
F/C1/300	'Feathery'	CMAS 1	300
F/C1/8	'Feathery'	CMAS 1	8
F/I/300	'Feathery'	Iceland VA	300
F/I/5	'Feathery'	Iceland VA	5
N/-/-	'Normal'	-	-
N/C1/300	'Normal'	CMAS 1	300
N/C1/5	'Normal'	CMAS 1	5
N/I/300	'Normal'	Iceland VA	300
N/I/5	'Normal'	Iceland VA	5
N/C2/300	'Normal'	CMAS 2	300
N/C2/5	'Normal'	CMAS 2	5

2.2. Erosion tests

The erosion tests were carried out at room temperature in an in-house built erosion test rig at the Technische Universität Dresden. The parameters for the erosion tests on the TBCs were based on the erosion experiments conducted by Wellman et al. [9]. Few changes in nozzle diameter and feeding rate guaranteed a smaller erosion spot size of 12.4 mm, necessary to adjust the erosion behavior to the particular samples. The modifications were chosen in a way to guarantee a comparable intensity of the particle jet to Wellman et al. [13] and are presented in Table 3.

Table 3 Erosion conditions of the used test rig compared to Wellman [31].

Erosion test rig operating conditions	Wellman	Current conditions
Temperature	RT	RT
Erodent	Alumina	Alumina
Particle Size [μm]	90-125	92.5 (d50)
Nominal velocity [m/s]	120	125
Impact angle	90°	90°
Feed rate [g/min]	0.5	0.25
Distance nozzle-sample [mm]	30	30
Nozzle diameter [mm]	9.5	5
Particle mass per erosion area and erosion time [$\text{mg}\cdot\text{mm}^{-2}\cdot\text{s}^{-1}$]	0.047	0.046
Energy of particle jet per erosion area and erosion time [$\text{mJ}\cdot\text{mm}^{-2}\cdot\text{s}^{-1}$]	0.34	0.36

Alumina particles with a size distribution of 54.5 μm (d10), 92.5 μm (d50) and 142.7 μm (d90) (Cilas, Cilas 1064) were used at a feeding rate of 0.25 g/min (Powder feeder GTV PF2/1, GTV Verschleißschutz GmbH). The particles were accelerated by a focused high pressure gas stream and reached a mean velocity of about 125 m/s (measured by a PIV system, PyroOptic Aps). They impinged on the coating at an impact angle of 90°. The distance between a nozzle of 5 mm diameter

and the specimen was 30 mm. The samples were weighed (Mettler Toledo Analytical Balances XA105DU) before the erosion test as well as in erosion intervals of 8x60 s for non-infiltrated samples. The measured intervals for infiltrated samples were changed to 6x60 s followed by 4x300 s. The short intervals detect the initial erosion effects, while the following long intervals minimize the error of measurement. Additionally, the coating volume loss for non-infiltrated samples was measured by confocal microscopy (μ scan; Nanofocus).

2.3. Characterization

All the tested samples were analyzed under a scanning electron microscope (SEM: DSM 982 Gemini, Zeiss). The CMAS infiltration zone was detected by analyzing the SEM-images in combination with energy dispersive X-ray-analysis (EDX: Noran System 7, Thermo Scientific). The areas undergoing a phase transition from $t' \rightarrow t \rightarrow$ monocline or $t \rightarrow$ cubic as well as those changing the crystallographic orientation were identified by electron backscatter diffraction (EBSD) measurements (SEM: Philips XL30; EBSD camera: Oxford Instruments). The potential of EBSD measurement to identify ZrO_2 phases was demonstrated by H. Berek et al. [32] at sintered TRIP-Matrix/ Mg-PSZ Composites. 5 micro hardness measurements (VMHT Fa. Uhl) per sample with a load of 300 g and Vickers indenter were done on the infiltrated samples on cross sections. The high load was chosen in order to measure the mean hardness of the coating by indent at least 3 columns per indentation [33].

3. Results and Discussion

3.1. Erosion tests

The coating volume loss over mass erodent exposure as well as erosion time for as-coated TBC is presented in Fig. 1. Infiltrated coatings depending on morphology, infiltration time and type of CMAS are presented Fig. 2. In both figures, the total coating volume/mass loss during the erosion test is presented as well as the slopes of the linear fitted erosion data (steady state erosion rate).

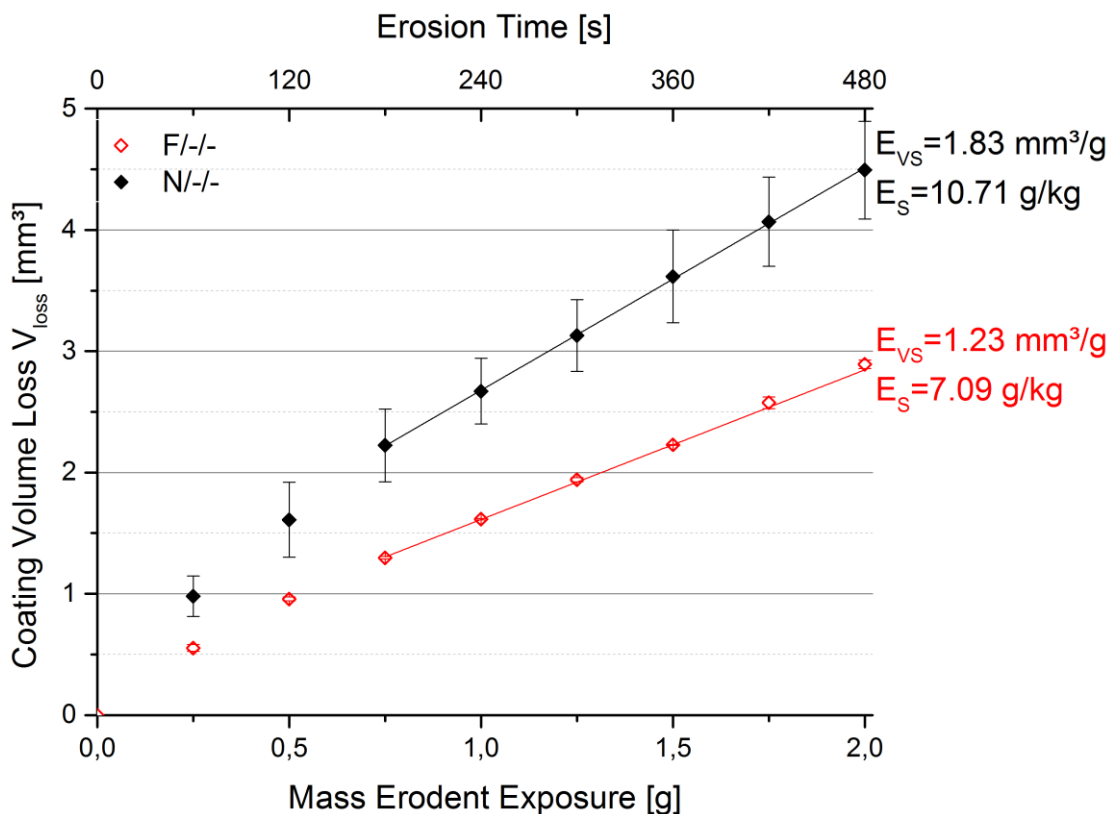


Fig. 1. Erosion data of as-coated F/-/- and N/-/- with coating volume loss plotted against erosion time as well as mass erodent exposure (slope of linear fitted erosion data as volumetric steady state erosion rate (E_{Vs}) and gravimetric steady state erosion rate (E_S))

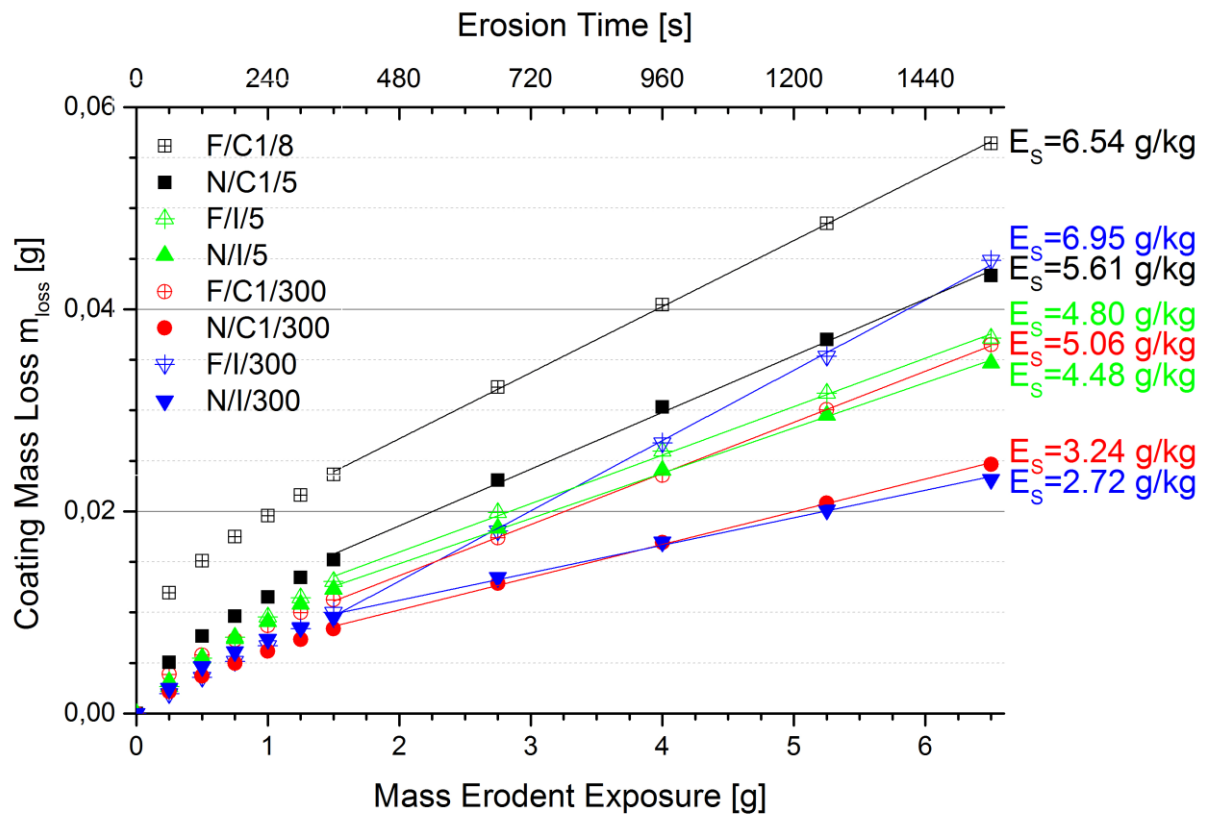


Fig. 2. Erosion data with coating mass loss plotted against erosion time as well as mass erodent exposure (slope of linear fitted erosion data as steady state erosion rate E_s)

Based on the different density of as-coated and infiltrated conditions, the erosion rate (coating mass loss vs. mass erodent exposure) should not be directly compared. Nevertheless, steady state erosion rates (E_s) of as-coated and infiltrated conditions are presented in Fig. 3 as usually seen in the literature for TBC with different densities [27]. Furthermore, a direct comparison between non-infiltrated and infiltrated samples should be based on the same heat-treatment. Since the steady state erosion rate of as-coated TBC already exceeded the infiltrated TBC in most cases, no aged TBC was tested because the ageing of the TBC structure leads to a further increase in the erosion rate [15]. However, only changes in the trends of the erosion behavior between as-coated and infiltrated samples are discussed in this paper.

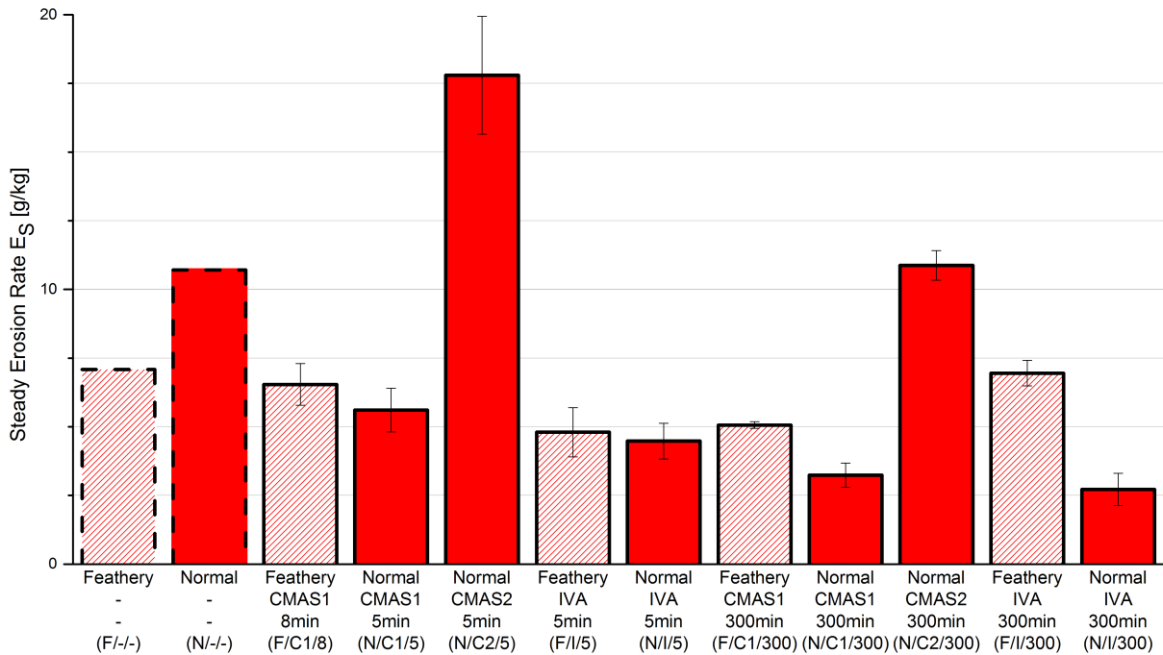


Fig. 3. Comparison of steady state erosion rates of as-coated TBCs (Fig. 1) and infiltrated TBCs (Fig. 2).

The high erosion rate at the beginning of the erosion test decreases with increasing erosion time until it reaches constant erosion rates after about 3 min for non-infiltrated TBC (Fig. 1) and 6 min for infiltrated TBC (Fig. 2). This high initial erosion rate for infiltrated TBC is due to the brittle CMAS depot above the coating's surface as well as the tips of the coatings intensely damaged by CMAS. Both effects do not describe the erosion behavior of the TBC itself, therefore the mass loss of the initial phase of the erosion test is not considered in Fig. 3.

Erosion rate non-/infiltrated 7YSZ

Depending on the microstructure the erosion rate of non-infiltrated samples varied between $E_{S, \text{Feathery}}=7.09$ g/kg and $E_{S, \text{Normal}}=10.71$ g/kg (Fig. 3). As shown, as-coated 'Feathery' structure has a higher erosion resistance compared to its counterpart, the 'Normal' structure. However, after infiltration the better erosion behavior was usually detected in the 'Normal' structure. The infiltration of the TBC by CMAS 1 and Iceland VA improved the erosion resistance which led to steady state erosion rates between 2.72 g/kg and 6.54 g/kg (Fig. 3). However, the steady state erosion rate after CMAS 2 infiltration ($E_{S, N/C2}=10.9-17.8$ g/kg) exceeded even non-infiltrated samples.

Comparable results from the literature were published by Wellman et al. with an erosion rate of ~10.9 g/kg (as-coated 7YSZ EB-PVD) [13] and ~9 g/kg (7YSZ EB-PVD with CMAS infiltration for 24 h/1500 °C) [26].

Influence of morphology on infiltrated 7YSZ

In contrast to the non-infiltrated TBCs ($E_{S, \text{Feathery}} < E_{S, \text{Normal}}$) it was found out that the infiltrated 'Feathery' morphology has a lower erosion resistance compared to the 'Normal' one. The long-term infiltrated 'Feathery' samples ($E_S=5.06-6.95$ g/kg) especially experienced a higher erosion rate compared to the 'Normal' counterpart ($E_S=2.72-3.24$ g/kg), as revealed in the high differences of its steady state erosion rate in Fig. 2. This constantly higher erosion rate results in an early failure of the long-term infiltrated 'Feathery' sample during erosion testing (Table 4) compared to its 'Normal' counterparts. The E_S of 'Feathery' and 'Normal' short-term infiltrated samples are identical for Iceland VA ($E_S=4.48-4.8$ g/kg) and similar for CMAS 1 ($E_S=5.61-6.54$ g/kg) during the erosion test.

Influence of heat treatment on infiltrated 7YSZ

Both the 'Normal' and 'Feathery' microstructures exhibit a general tendency of increased erosion resistance with respect to the increase in the infiltration time which was shown in Fig. 5. For example,

Fig. 2 presents that the total coating mass loss (m_{loss}) as well as the steady state erosion rate of short-term infiltrated 'Normal' samples ($m_{\text{loss};N/C1/5}=0.0433$ g; $E_{S;N/C1/5}=5.61$ g/kg) are higher compared to long-term infiltrated samples ($m_{\text{loss};N/C1/300}=0.0246$ g; $E_{S;N/C1/300}=3.24$ g/kg). The Iceland VA infiltrated 'Feathery' samples are the only exception in this test series where the erosion resistance of long-term infiltrated is higher than its short-term infiltrated sample.

Influence of CMAS/Iceland VA composition on infiltrated 7YSZ

The tested compositions of CMAS/Iceland VA have shown different impacts on the erosion behavior of the 7YSZ coatings. CMAS 1 ($E_{S;N/C1/300}=3.24$ g/kg) leads to a slightly higher erosion rate compared to Iceland VA ($E_{S;N/I/300}=2.72$ g/kg) except for the long-term infiltrated 'Feathery' sample. Additionally, CMAS 2, tested only on 'Normal' samples, leads to a very high erosion rate ($E_{S;N/C2/300}=11.13$ g/kg) compared to the other compositions. The early failure of the CMAS 2 (Table 4) infiltrated coatings suggests a more intense attack of the TBC. CMAS 2 on 'Feathery' samples are currently investigated.

Table 4 Time of occurrence of TBC delamination during erosion test defined as failure of the coating

Sample designation	Time to TBC failure during erosion test [s]
F/C1/300	1770
F/C1/8	2220
F/I/300	1560
F/I/5	2130
N/C1/300	>4260
N/C1/5	1920
N/I/300	>4260
N/I/5	3220
N/C2/300	1260
N/C2/5	960

3.2. Micro hardness

The micro hardness measurements were conducted on cross-sectioned infiltrated 7YSZ-EB-PVD TBCs in the middle of the coating (at a distance of 200 μm to the substrate). The high relative standard deviation ($\pm 29\%$) that were reported by Wellman et al. [33] for nano indentation on cross section of EB-PVD TBC, was not observed in this study (Fig. 4), except for F/C1/8. Wellman tested as-coated EB-PVD TBC which led to a lateral movement of the columns during indentation. The CMAS infiltration of the TBC might be the reason for the lower deviation in this work. The fully infiltrated CMAS stabilizes the TBC columns and inhibit the flexibility and bending of the columns during indentation. The micro hardness of all samples was found to vary between 1010 HV0.3 and 1125 HV0.3. A decrease in the micro hardness leads to an increase in the erosion rate, as represented in Fig. 4, similarly to findings in [13]. There is no clear trend or correlation between micro hardness and morphology/ duration of CMAS infiltration/ CMAS composition. The phase changes discussed in 3.4 seem to have no systematic influence on the micro hardness.

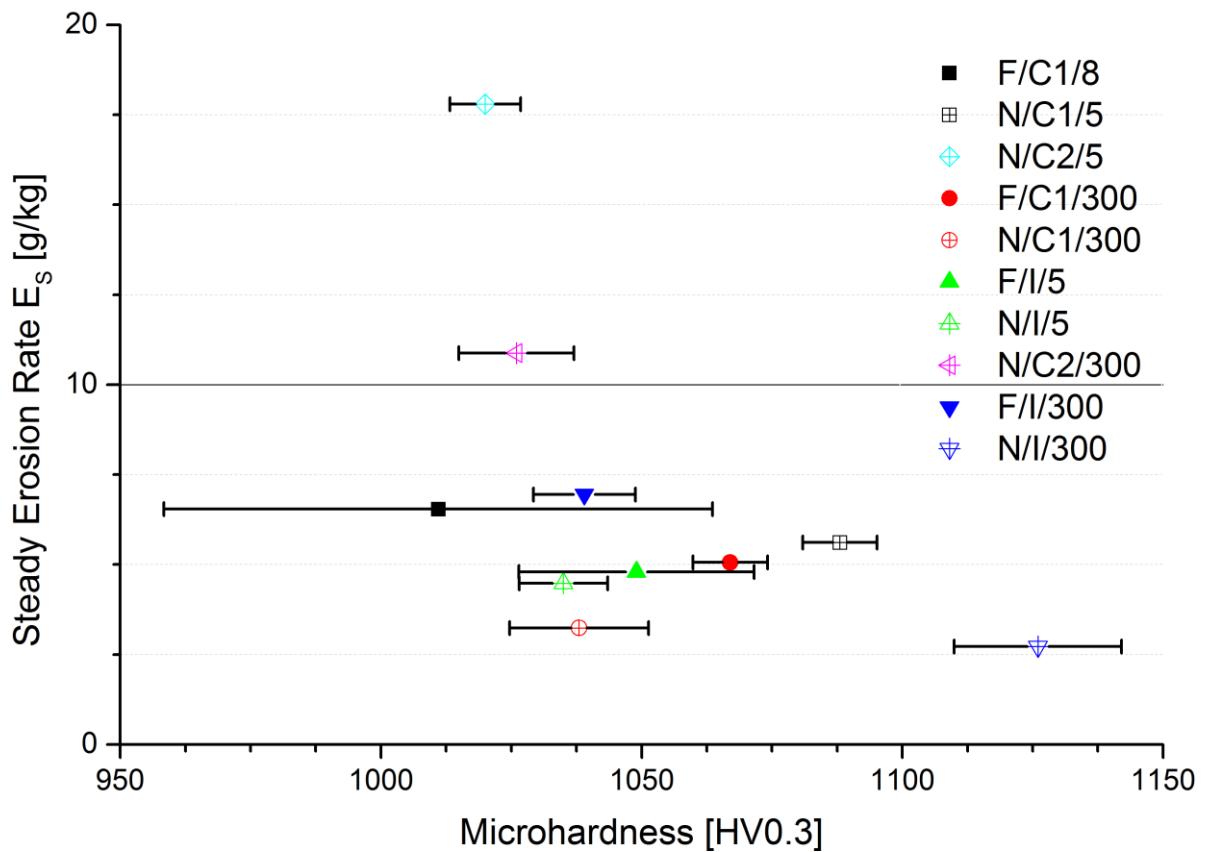


Fig. 4. Steady state erosion rate plotted against micro hardness HV0.3.

3.3. Erosion behavior of as-coated 'Feathery' and 'Normal' structure

The influence of morphology on the erosion behavior of non-infiltrated EB-PVD 7YSZ coatings is presented in this section. The columns of the 'Feathery' structure are 50 % finer than the 'Normal' ones, which leads to an increased amount of open channels and a higher porosity, however, at the same time feather arm lengths are 1/2th of the column diameter compared to the 1/6th of the column diameter ('Normal' structure) which was shown in the literature [27].

The results show that the as-coated 'Feathery' structure has a superior erosion behavior compared to the 'Normal' structure (Fig. 1). After a high erosion rate in the initial phase of the erosion test, it decreases for both morphologies to a constant level of erosion. The steady state erosion rates of N/-/ ($E_{S'Normal}=10.71$ g/kg) is comparable to experiments made by Wellman et al. [13] on as-received standard 7YSZ EB-PVD (10.9 g/kg). Furthermore, they investigated that low density t'-7YSZ leads to a lower thermal conductivity but also to higher erosion rates. The lower density was achieved by more distinctive feather arms compared to the standard samples. The changed microstructure was held responsible for the higher erosion rate (14.83 g/kg) at room temperature. In contrast, erosion tests in this study on high porosity F/-/ reveal that the erosion behavior improved ($E_{S'Feathery}=7.09$ g/kg), although the length of the feather arms increased. The superior erosion behavior of the 'Feathery' structure can be explained by the finer columns. The material loss by a cracked column will be less for a smaller column diameter. Since the column boundary is a natural barrier for crack propagation, the impacts of erosion particles have to initiate cracks in multiple columns of the 'Feathery' structure [14]. In addition to the explained effect, the reduced gap width of the 'Feathery' structure (1-1.2 μ m) compared to the 'Normal' (1.7-2.3 μ m) has to be considered [27]. A particle that impinges in any off-axis symmetry to the columns can cause bending of the columns [34]. The lower gap width enables the neighboring columns to support the bended column more intensively. The maximal bending of a particular column is reduced and the force, applied by the particle impact, is initiated into the TBC more fordable. The images in Fig. 5 support this argument. While the columns of the 'Normal' structure cracked near the surface as well as at a depth of 192 μ m, the 'Feathery' structure showed only erosion damage close to the surface (44 μ m). The expected high amount of cracks initiated at the strongly pronounced feather arms (also known as dendrites by Wellman et al. [35]) of the 'Feathery' structure

can be observed in Fig. 6. Nevertheless, this kind of crack initiation can be detected in both types of morphologies.

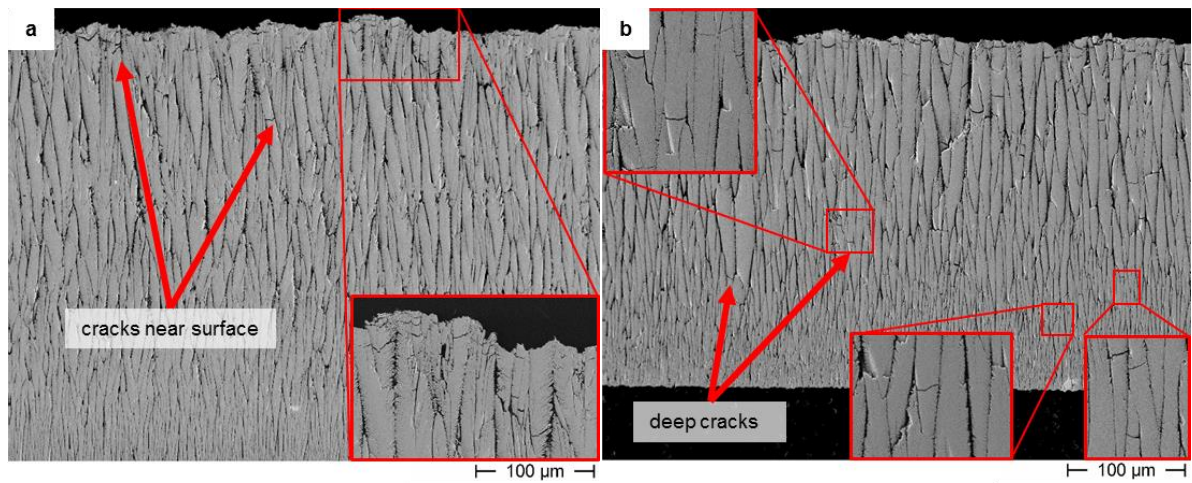


Fig. 5. Overview of erosion damage on TBC a) erosion on 'Feathery' structure (F/-/-), b) erosion on 'Normal' structure (N/-/-).

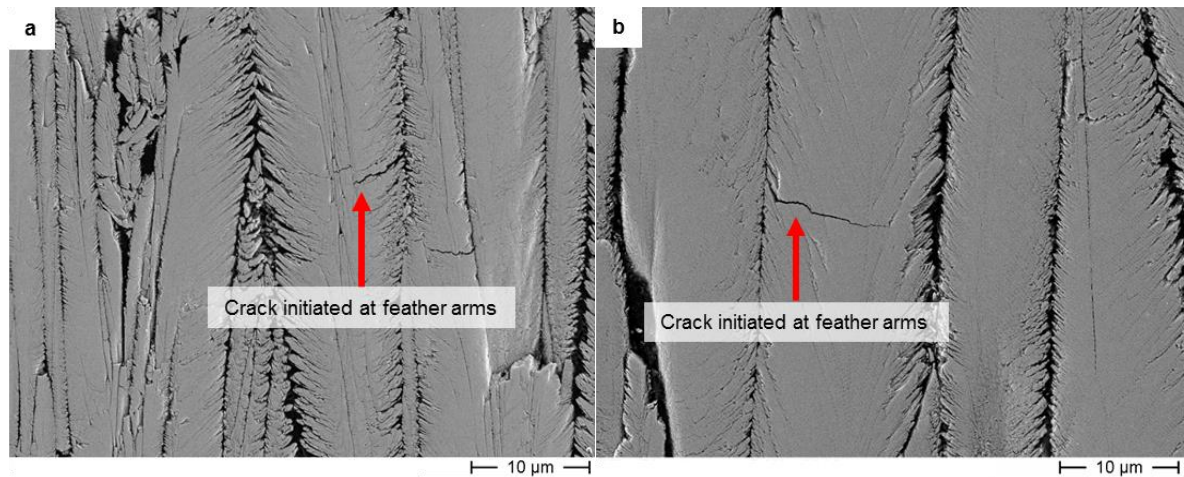


Fig. 6. Crack initiated at the longer feather arms of a) the 'Feathery' structure (F/-/-) and b) the 'Normal' structure (N/-/-).

3.4. General degradation and erosion behavior of infiltrated specimens

Degradation of 7YSZ due to the CMAS attack

During the infiltration of the TBC by CMAS, the gaps between the columns as well as the feather arms of the columns were penetrated. While the short-term infiltration only leads to a full infiltration of all accessible open channels in the TBC, a longer annealing time initiates a pronounced phase transformation of the ZrO_2 based on the depletion of Yttrium, too. From the literature it is known that near the CMAS depot, metastable tetragonal- ZrO_2 (t' - ZrO_2) transforms into monoclinic ZrO_2 (m - ZrO_2) while a transformation from t' - ZrO_2 into cubic ZrO_2 (c - ZrO_2) mainly occurs close to the substrate [5]. This transformation can partly reveal closed porosity for CMAS infiltration.

EBSD measurements (Fig. 7) in this study reveal that a phase transformation happened during the heat treatment for 300 mins. However, the cubic phase is formed at the interface of CMAS and YSZ and it also exists at the gaps between the columns as well as in the feather arms. The cubic phase is detected even at the sharp end of the feather arms. In general, the t' -phase transforms to a

mixture of monoclinic + cubic phases [29]. Due to its lower presence and finer distribution, the m-phase could not be verified by the EBSD measurement. However, the detected c-phase might be linked to the presence of the m-phase. Isolated c-phase points in Fig. 7 b may be due to measurement errors, but multiple points of c-phase especially in areas of good pattern quality strongly indicate its presence. Additional measurements and TEM investigations are currently being conducted to confirm the c-phase as well as to detect and evaluate the m-phase after 300 min of heat treatment which will be the topic of a future publication. Furthermore, the EBSD images in Fig. 7 show t-phase around the detected c-phase, which has a different crystallographic orientation than the large columnar crystals. This indicates that during the long-term heat treatment at 1250 °C the t' phase has transformed into t + c-phase with the possible addition of non-detectable monoclinic phase.

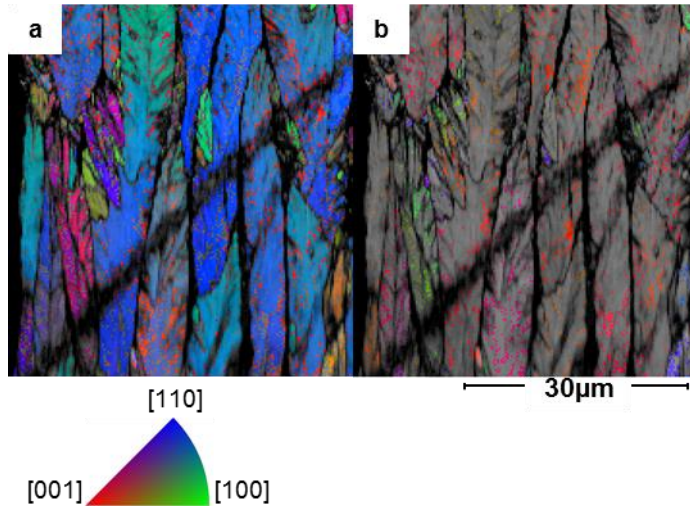


Fig. 7. EBSD measurement of the middle part of F/C1/300 sample. Greyscale pattern quality image with overlay of orientation mappings of the t'/t-ZrO₂-Phase (a) and the c-ZrO₂-Phase (b) with respect to sample normal (color key).

The phase transformation in 7YSZ leads to a change in fracture toughness and micro hardness, which is essential to the erosion behavior of the coating [13]. In general, the m-ZrO₂ ($K_{Ic}=2-2.6 \text{ MPa}\cdot\text{m}^{1/2}$) and the c-ZrO₂ ($K_{Ic}=1-2 \text{ MPa}\cdot\text{m}^{1/2}$) have a lower fracture toughness than the initial t'-Phase ($K_{Ic}=3 \text{ MPa}\cdot\text{m}^{1/2}$) [36,37]. F. F. Lange [38] and A. Loganathan et al. [39] have shown that an increase in volume fraction of the m-ZrO₂ as well as c-ZrO₂ leads to a decrease in fracture toughness. The fracture toughness (K_{Ic}) of pure CMAS varies between 0.6-2.0 $\text{MPa}\cdot\text{m}^{1/2}$, which leads to the assumption of a further weakening of the coating [40,41].

General erosion behavior of infiltrated 7YSZ-EB-PVD

The CMAS infiltration in the TBCs and partly the sintering effect at 1250 °C [42] has led to a network of vertical cracks in the long as well as short-term infiltrated samples before they were exposed to erosion as shown in Fig. 8 a [10]. Those cracks are weak areas in the TBC and vulnerable to the erosion particle as it is shown in Fig. 8 b. During the erosion attack, the first material removal takes place at those cracks. The infiltrated columns nearby those cracks are not fully surrounded by next adjacent columns which results in less support during the erosion as described previously (Fig. 9). Those columns, which fracture first cannot be supported by the missing adjacent columns [12]. The removal of the columns exposes new columns leading to a widening of the cracks over erosion time (Fig. 9), a hilly surface and in the end to a comparable flat erosion surface, as shown in Fig. 8 b.

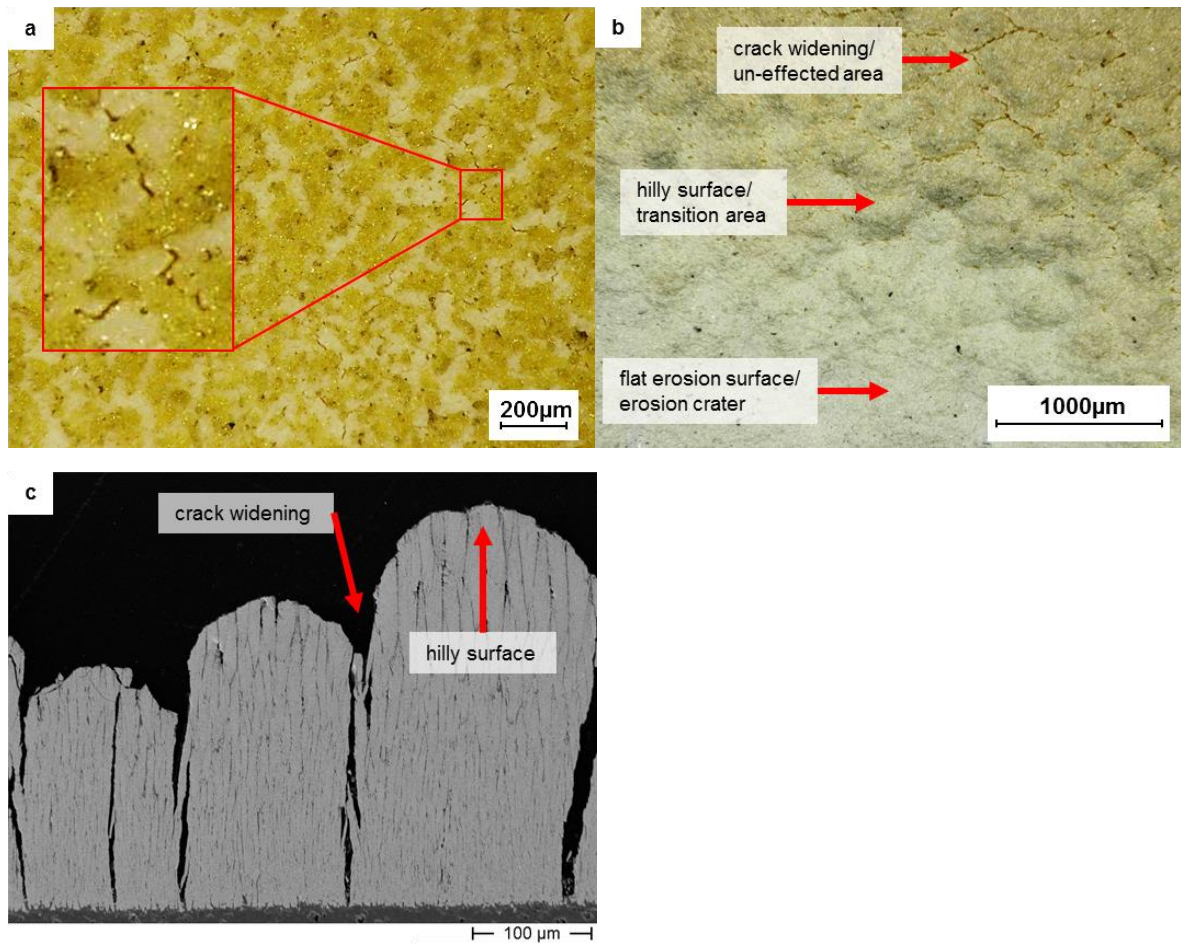


Fig. 8. Stereomicroscope images of pronounced vertical crack network (F/C1/300) a) as a consequence of the CMAS infiltration, b) after erosion exposure for 360 s and c) SEM image of cross section of those cracks after erosion testing for 360 s.

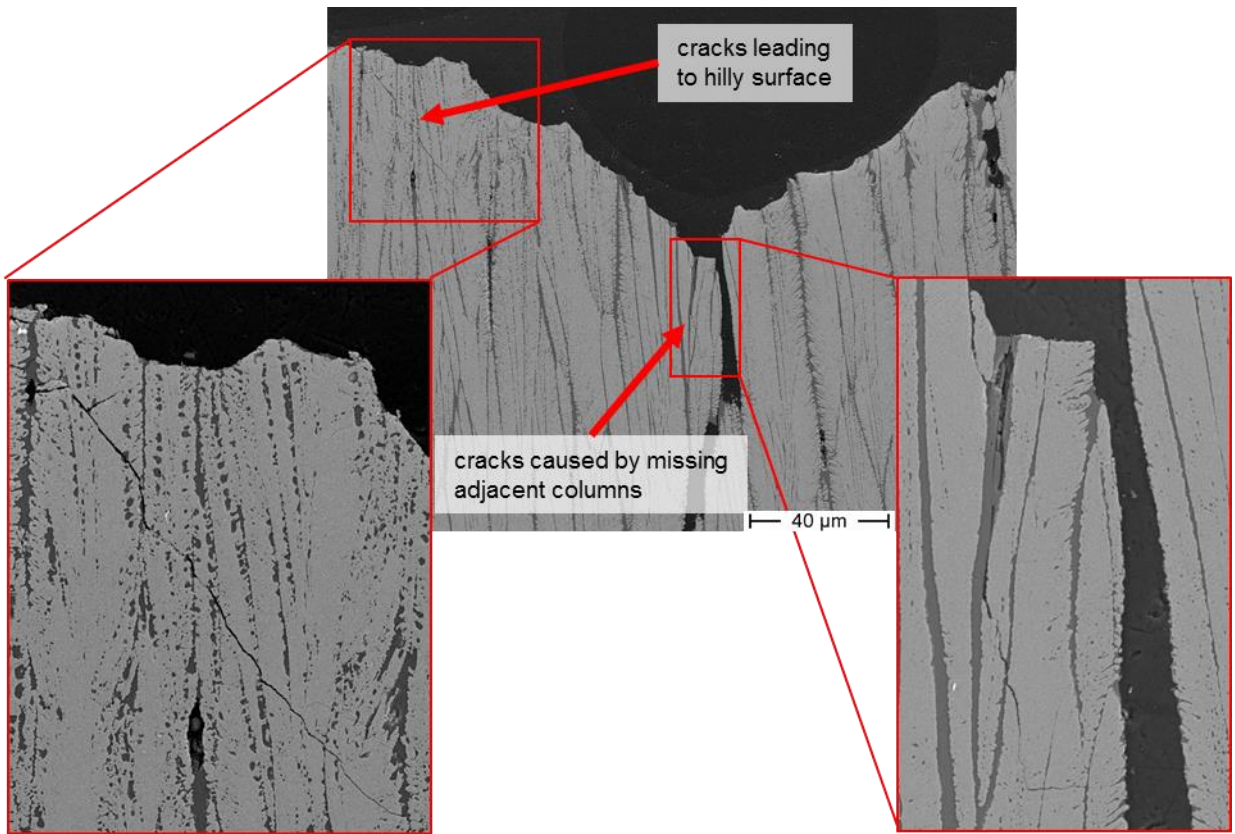
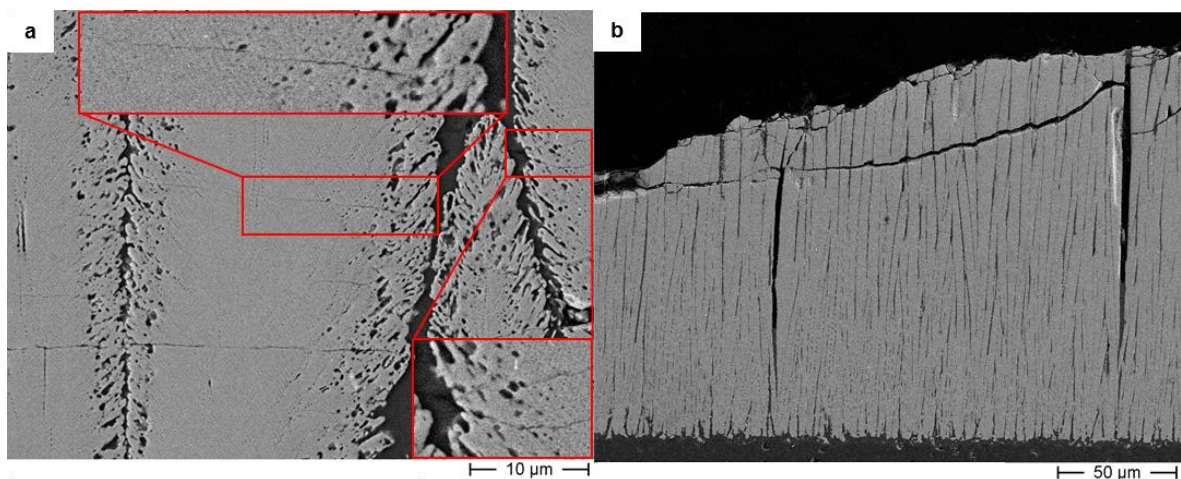


Fig. 9. Missing adjacent columns erosion mechanism responsible for hilly surface (F/C1/8)

Crack initiation frequently occurs at the microstructure of the feather arm caused by the notching effect and its stress concentration (Fig. 10 a). SEM images (Fig. 10 c-d) show that the main cracks can be observed in the first 30 µm parallel to the coating's surface in both morphologies. Being caused by the infiltrated columns, cracks do not stop at the column boundaries but propagate through the CMAS-infiltrated area to neighboring columns (Fig. 10 b). The infiltrated TBC behaves like a bulk material. A removal of material only occurs if the cracks reach the TBC surfaces or each other. The removed material exposes the layer underneath to the following erosion particles which leads to new cracks and material removal. This erosion effect is in accordance to the observations by Wellman et al. [26] as well as Steenbakker et al. [37].



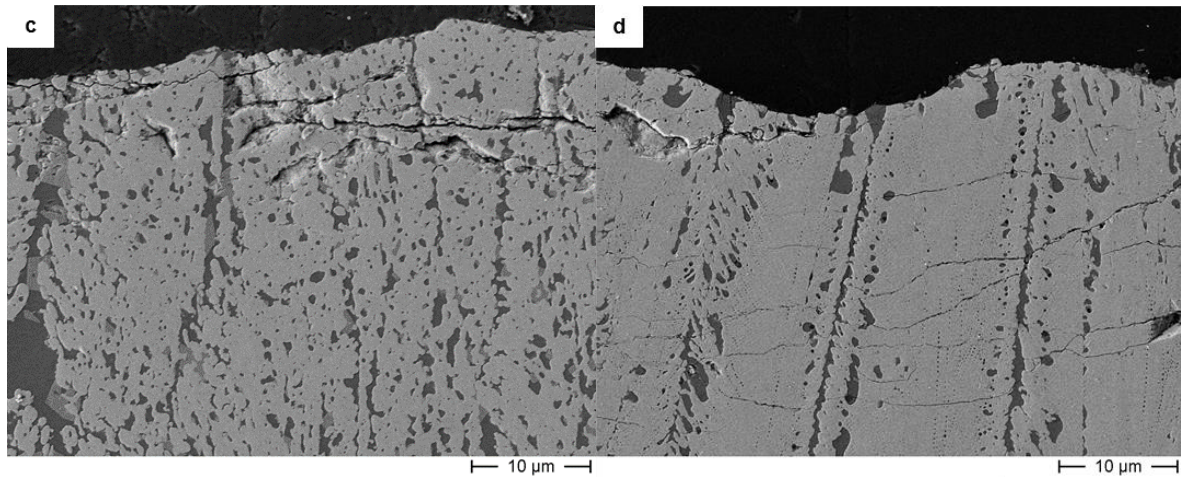
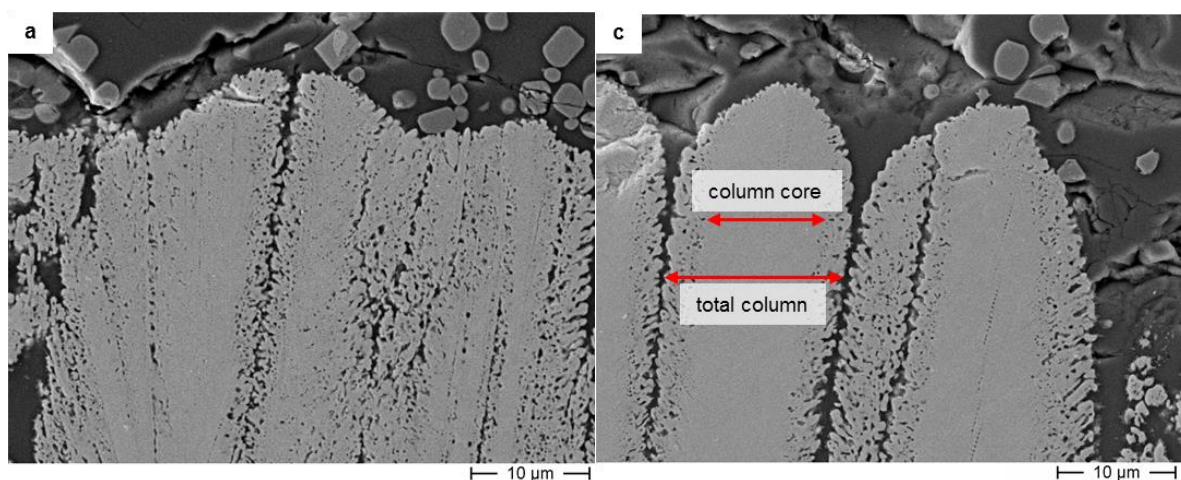


Fig. 10. a) N/C1/5 Crack initiation at feather arms infiltrated by CMAS; b) N/C2/300 crack propagation through adjacent columns; c) F/1/300 and d) N/C1/300 micro cracks in the upper 30 μm of the eroded coating independently of the morphology.

3.5. Influence of morphology, CMAS composition and heat treatment on erosion behavior

Influence of morphology

The longer feather arms of the 'Feathery' samples lead to a high specific surface area which enables the CMAS to infiltrate deeply into the columns. The longer feather arm gaps were subjected to deeper penetration of the CMAS which went through rigorous reaction and enhanced the dissolution process of the t'-phase and the re-precipitation of the t- and c-phase after the 300 min annealing. The dissolution process leads to a complete degradation of the feather arms and is presented by the effect of Iceland VA after long-term infiltration on the tip of the 'Feathery' 7YSZ columns in Fig. 11 b. In comparison Iceland VA has infiltrated into the shorter feather arms of the 'Normal' structure which in turn reacted only with the frame of the columns and leaves the column core stable. The differences in the microstructural features between 'Feathery' and 'Normal' is represented schematically in Fig. 12. The extended feather arms in case of 'Feathery' have undergone to a complete destruction of the 'Feathery' structure after 300 min of Iceland VA infiltration as demonstrated in Fig. 11 c whereas a clear presence of unreacted core of the column is still sustained after 300 min of infiltration in the 'Normal' structure (see Fig. 11 d). The higher rate of decomposed t'-columns (also the increase in volume fraction of brittle c-phase) has led to an increased erosion rate of the 'Feathery' structure compared to the 'Normal' structure. The column core of the latter consists still of unreacted t' phase with a higher fracture toughness which ultimately leads to a lower erosion rate. A similar behavior can be observed in the middle section of the Iceland VA infiltrated 'Feathery' TBC as shown in Fig. 14 b-c.



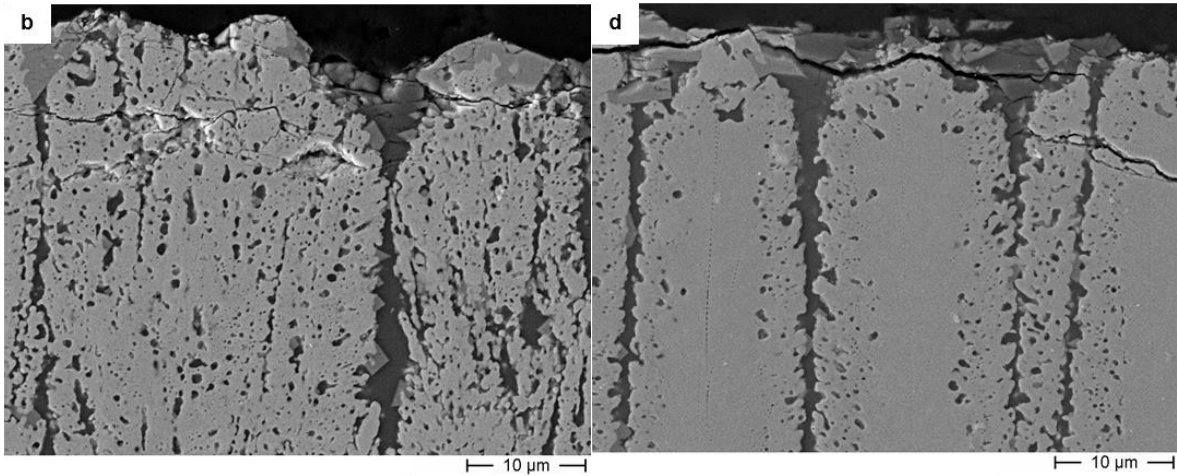


Fig. 11. SEM images of the TBC tips for comparison of the remaining unreacted inner column cores a) F/I/5, b) F/I/300, c) N/I/5, d) N/I/300.

Influence of heat treatment

Based on the erosion data presented in Chapter 3.1 one can conclude that long-term infiltrated TBCs have a better erosion resistance than short-term infiltrated once. The influence of the infiltration time on the erosion behavior can be understood by taking a deeper look at the remaining unreacted column core presented schematically in Fig. 12. The porosity of the tough t'-columns are partly filled by brittle CMAS and phase transformations occur mainly in those regions. Those areas are believed to be generally responsible for a lower erosion resistance. The 'Normal' structure retains an inner t'-column independently of the infiltration time (due to the larger column diameter and lower porosity). However, at the tip of the column the remaining unreacted column core ratio is thinner after 300 min of infiltration compared to the 5 min of infiltration. In the middle and the lower middle sections of the coating (along the thickness), the remaining unreacted column core ratio of the short-term and the long-term infiltration is nearly equal (see Fig. 13). This fact leads to the expectation of a comparable erosion rate but it does not explain the constantly lower erosion rate of the long-term infiltrated 'Normal' samples.

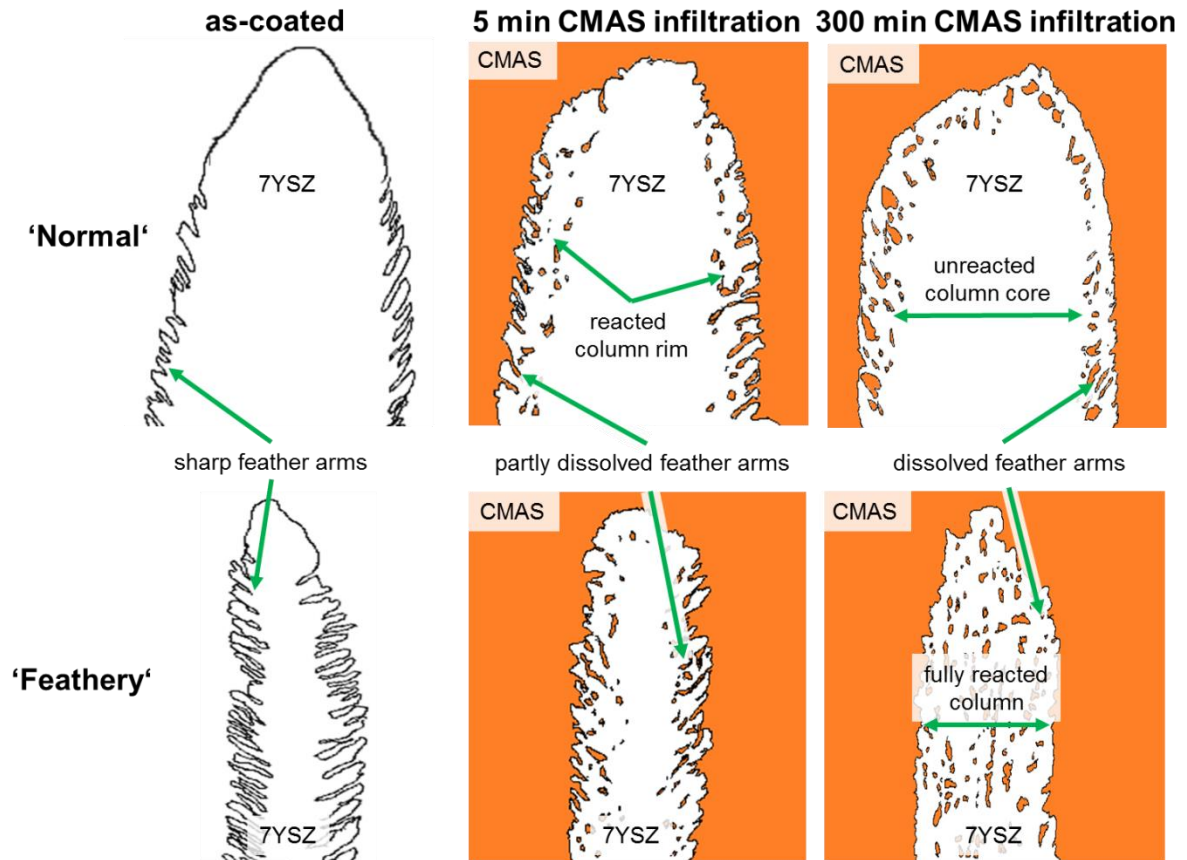


Fig. 12. Schematic representation of TBC column tips microstructure changes during CMAS infiltration and annealing at 1250 °C

It is believed that the crack initiation mainly occurs at the microstructure of the feather arms because of stress concentration, as mentioned in chapter 3.4 and illustrated in Fig. 10 a. The notching effect results from the existence of different TBC-phases (t' -, c -, m -ZrO₂) at the same location, their shape, specific properties such as elastic modulus, hardness, and toughness, and finally the CMAS presence which in turn creates an inhomogeneous stress field in the TBC during erosion. Especially at columns which are not fully surrounded by the next adjacent columns caused by cracks after CMAS infiltration, an initiation of horizontal cracks occurs by the notching effect (Fig. 9). The crack propagates through several columns caused by the bulk material erosion behavior (Fig. 10 b). This results in the removal of columns and leads to the characteristic erosion surface discussed in 3.4 and presented in Fig. 8 b.

Though the remaining unreacted column core ratio is nearly equal in the middle section, Fig. 13 reveals the progressive dissolving of the feather arms of this TBC section over heating time at 1250 °C. It is caused by both the sintering effect and dissolution by CMAS. Closed porosity and decreasing feather arms lengths from the tip to the bottom leads to a less deep CMAS infiltration into the columns [5]. The stress concentration and consequently, the notching effect reduces if the shapes of the feather arms change from sharp to round shapes as happened during the heat treatment and is demonstrated in Fig. 12. This dissolving effect during the heat treatment improves the erosion behavior of the long-term infiltrated 'Normal' structure.

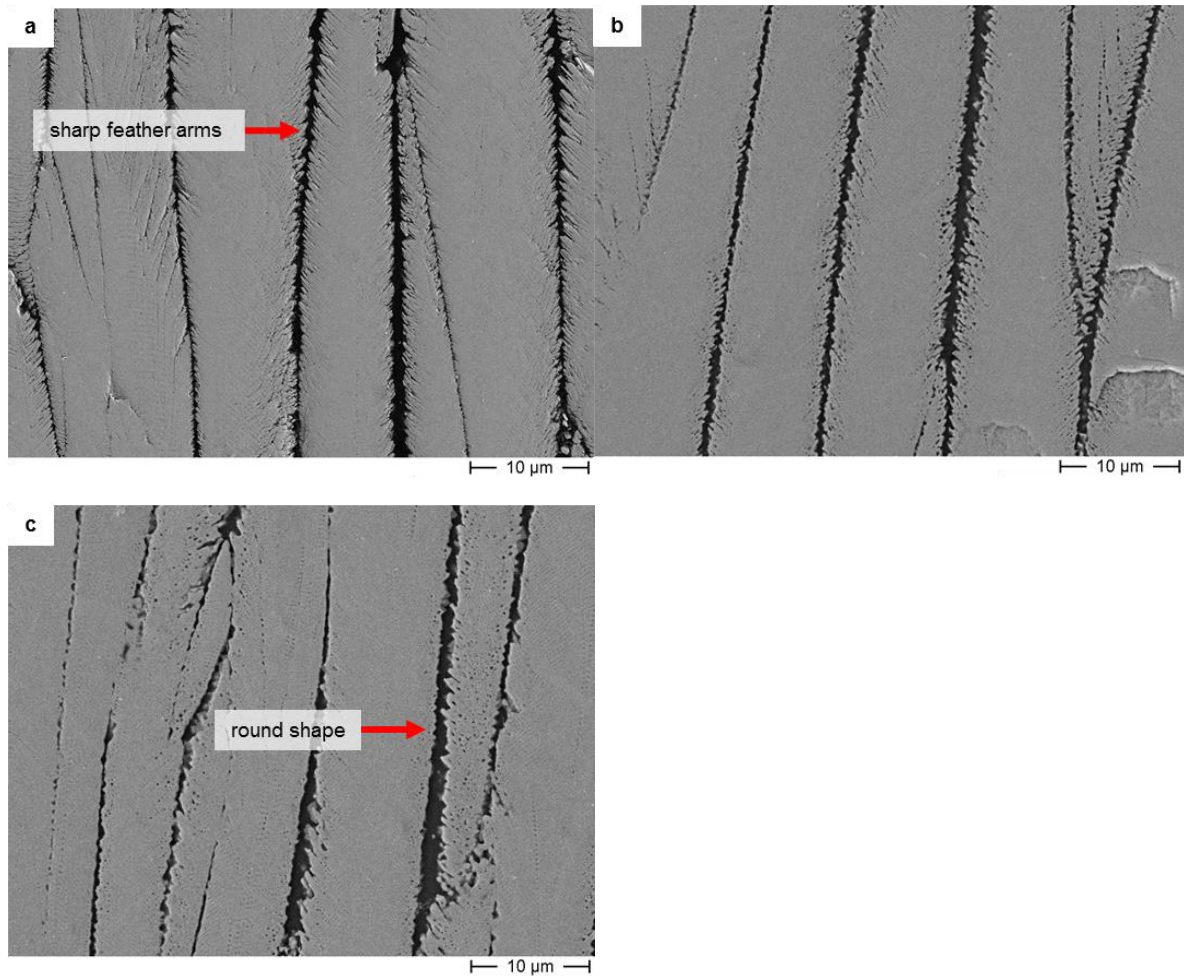


Fig. 13. Constant remaining unreacted column core ratio while change of the shape of feather arms in the middle section of TBC caused by Iceland VA infiltration and infiltration time a) N/-; b) N/I/5; c) N/I/300.

Concerning the 'Feathery' structure and its pronounced feather arms, the notching effect has a high impact on the erosion behavior. Furthermore, the decline of the unreacted column core towards a fully reacted column also influences the erosion resistance. A schematic illustration of the change in microstructure of 'Feathery' samples is given in Fig. 12. F/C1 improves its erosion resistance with respect to the increase in infiltration time. This trend is similar to the 'Normal' structure. The damage to the column core caused by CMAS infiltration is less intense at the middle sections of the coating compared to the tip sections. Though the remaining unreacted column core ratio is declining, the reduction of the notching effect by dissolving the sharp feather arms leads to the improved erosion resistance (Fig. 14 c). Due to the lower viscosity of CMAS1 compared to Iceland VA, the feather arms have undergone an advanced dissolution process. In contrast to F/C1, the erosion resistance of F/I declines with respect to the increase of infiltration time (see Fig. 3). The high viscosity of volcanic ash prevents the feather arms of a deep infiltration and consequently no advanced dissolution process occurs. As revealed in Fig. 14 b the sharp feather arms of F/I/300 are not completely dissolved after 300 min at 1250 °C. Hence the notching effect is not reduced significantly compared to F/I/5 (see Fig. 14 a). The explanation of the increasing erosion rate of F/I/300 might be the remaining unreacted column core ratio. As it is shown in Fig. 11 a, the remaining column core of the tip of short-term infiltrated 'Feathery' TBC is thin. At the latest, after 300 min at 1250 °C this thin column core has completely vanished. Furthermore, the middle part of the TBC also contains less reacted column core after short-term than after long-term infiltration (Fig. 14 a-b), which is responsible for the discussed trend of the Iceland VA infiltrated 'Feathery' erosion rate ($E_{S;F/I/5}=4.80 \text{ g/kg} < E_{S;F/I/300}=6.95 \text{ g/kg}$).

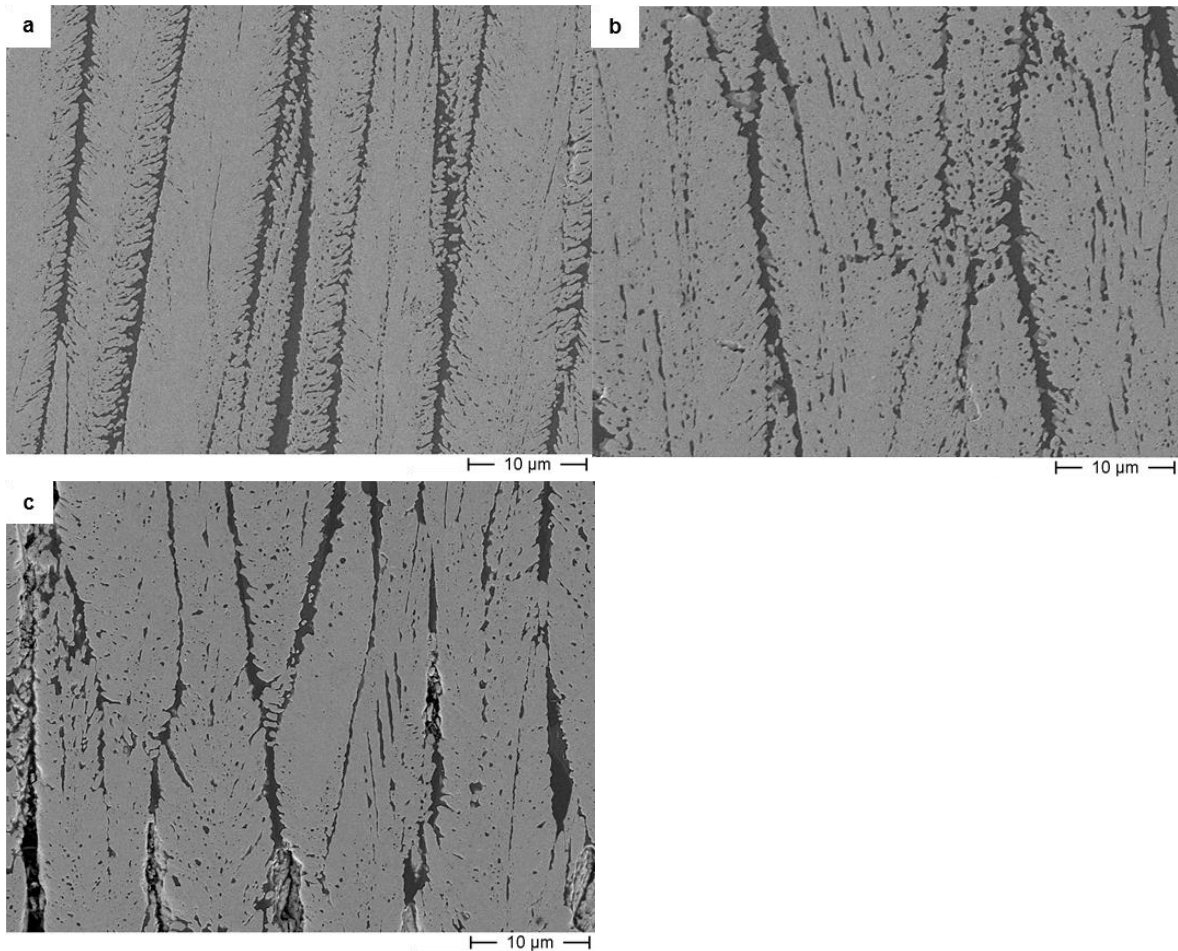


Fig. 14. SEM images of the TBC middle part for comparison of the remaining unreacted column cores and change of shape of feather arms caused by Iceland VA/CMAS infiltration and infiltration time a) F/I/5; b) F/I/300; c) F/C1/300.

Influence of CMAS/Iceland VA composition

Concerning the influence of CMAS composition on the erosion behavior, the melting point of CMAS 2 is 10-20 °C below the melting point of CMAS 1 (Table 1). The lower melting point of CMAS 2 accommodates more time for the infiltration in the TBC which might lead to a longer time for degradation compared to CMAS 1. Additionally, the low viscosity enables the CMAS 2 to infiltrate deeply into the tiniest pores of the TBC columns (Table 1). The combination of both effects results into a higher degradation grade of the TBC as well as a pronounced re-precipitation of the t- and c-phase. The consequentially declining fracture toughness explains the high erosion rate of CMAS 2 infiltrated TBC with 'Normal' structure (Fig. 3), which was expected since the CMAS 2 is known to be more reactive compared to CMAS 1 and Iceland VA [29].

The infiltration behavior of Iceland VA and CMAS 1 is different. The lower melting point of Iceland VA (Table 1) enables to infiltrate the coating already during the heating-up phase of the furnace. This leads to a longer time of degradation during the annealing, especially during the short-term infiltration. Having the higher viscosity (higher SiO₂ content) it infiltrates slowly and has enough time in dissolving the tip of the columns but in the middle sections closed porosity was still non-infiltrated. At the same time, the lower viscosity of CMAS-1 enables it to penetrate into the TBC columns more deeply [30]. Hence it may lead to a higher phase transformation towards brittle phases but also results in a pronounced dissolving of the sharp feather arms as shown in Fig. 14 b-c) (F/I/300 compared to F/C1/300). In most cases the intense phase transformation of CMAS-1 leads to a higher erosion rate. The difference between the CMAS compositions concerning chemical degradation and erosion behavior is the topic of on-going research.

4. Conclusions

The influence of coating morphology, CMAS composition, and infiltration time at 1250 °C on the room temperature erosion behavior of EB-PVD 7YSZ TBCs was studied.

The erosion behavior of the as-coated 'Feathery' structure is superior to the as-coated 'Normal' structure because:

- Finer columns of the 'Feathery' structure require cracks in multiple columns to guarantee material loss.
- Lower gap width between columns minimizes the total bending of columns during off-axis impacts.
- The notch effect is overcompensated by the finer column shape, although more and deeper feather arms are present within 'Feathery'.

Secondly, infiltration of the TBC by CMAS or volcanic ash lowers the erosion rate slightly (feathery structure) or greatly (normal structure). The reasons for this behavior are:

- Infiltrated TBC behaves as continuum material during erosion exposure.
- The main erosion damage is surface spallation.

After CMAS infiltration the 'Normal' structure showed a superior erosion resistance compared to the 'Feathery' structure. The reversed order of erosion resistance compared to the as coated condition is based on the influence of morphology, heat treatment and CMAS composition on the erosion behavior. The main findings are summarized as followed:

- Long feather arms allow deep infiltration of CMAS into columns and phase transformation is much more pronounced in 'Feathery'.
- Within the same microstructure the erosion resistance increases slightly due to the reduction of the notching effect during the heat treatment.
- Chemical composition and viscosity defines the degradation of the TBC and hence the toughness and erosion behavior.

Since the 'Feathery' structure retards the CMAS infiltration and has a lower thermal conductivity [27], the non-infiltrated part of the 'Feathery' TBC under realistic circumstances in a gas turbine (with a thermal gradient as in the case of a real blade) is larger compared to the 'Normal' structure. For this reason a superior erosion resistance of the 'Feathery' structure can be expected for partly CMAS-infiltrated TBCs under realistic turbine conditions.

Acknowledgment

The authors thank the German Science Foundation (DFG) for funding this project (project no. LE 1373/34-1, SCHU 1372/5-1). The technical assistance of P. Lutze at TU Dresden as well as helpful technical discussions with D. Eichner and A. Nehls is acknowledged. The authors express their gratitude to D. Peters and J. Brien for manufacture of TBCs, as well as A. Handwerk for providing technical support for thermal test implementation.

References

- [1] G. Pujol, F. Ansart, J.-P. Bonino, A. Malié, S. Hamadi, Step-by-step investigation of degradation mechanisms induced by CMAS attack on YSZ materials for TBC applications, *Surface and Coatings Technology*. 237 (2013) 71–78. doi:10.1016/j.surfcoat.2013.08.055.
- [2] N.P. Padture, M. Gell, E.H. Jordan, Thermal barrier coatings for gas-turbine engine applications, *Science*. 296 (2002) 280–284.
- [3] A.G. Evans, D.R. Clarke, C.G. Levi, The influence of oxides on the performance of advanced gas turbines, *Journal of the European Ceramic Society*. 28 (2008) 1405–1419. doi:10.1016/j.jeurceramsoc.2007.12.023.
- [4] N. Marchand, R.M. Pelloux, A computerized test system for thermal-mechanical fatigue crack growth, *Journal of Testing and Evaluation*. 14 (1986) 303–311.
- [5] S. Krämer, J. Yang, C.G. Levi, C.A. Johnson, Thermochemical Interaction of Thermal Barrier Coatings with Molten CaO–MgO–Al₂O₃–SiO₂ (CMAS) Deposits, *Journal of the American Ceramic Society*. 89 (2006) 3167–3175. doi:10.1111/j.1551-2916.2006.01209.x.

- [6] R. Naraparaju, P. Mechnich, U. Schulz, G.C. Mondragon Rodriguez, The Accelerating Effect of CaSO₄ Within CMAS (CaO–MgO–Al₂O₃–SiO₂) and Its Effect on the Infiltration Behavior in EB-PVD 7YSZ, *J. Am. Ceram. Soc.* 99 (2016) 1398–1403. doi:10.1111/jace.14077.
- [7] C. Mercer, S. Faulhaber, A.G. Evans, R. Darolia, A delamination mechanism for thermal barrier coatings subject to calcium–magnesium–alumino-silicate (CMAS) infiltration, *Acta Materialia*. 53 (2005) 1029–1039. doi:10.1016/j.actamat.2004.11.028.
- [8] R. Darolia, Thermal barrier coatings technology: critical review, progress update, remaining challenges and prospects, *International Materials Reviews*. 58 (2013) 315–348. doi:10.1179/1743280413Y.0000000019.
- [9] R.G. Wellman, J.R. Nicholls, A review of the erosion of thermal barrier coatings, *Journal of Physics D: Applied Physics*. 40 (2007) R293–R305. doi:10.1088/0022-3727/40/16/R01.
- [10] H. Peng, L. Wang, L. Guo, W. Miao, H. Guo, S. Gong, Degradation of EB-PVD thermal barrier coatings caused by CMAS deposits, *Progress in Natural Science: Materials International*. 22 (2012) 461–467. doi:10.1016/j.pnsc.2012.06.007.
- [11] A. Grini, G. Myhre, C.S. Zender, I.S.A. Isaksen, Model simulations of dust sources and transport in the global atmosphere: Effects of soil erodibility and wind speed variability, *J. Geophys. Res.* 110 (2005) D02205. doi:10.1029/2004JD005037.
- [12] R. Wellman, J.R. Nicholls, A mechanism for the erosion of EB PVD TBCs, in: *Materials Science Forum*, Trans Tech Publ, 2001: pp. 531–538. <http://www.scientific.net/MSF.369-372.531.pdf> (accessed June 14, 2016).
- [13] R.G. Wellman, J.R. Nicholls, K. Murphy, Effect of microstructure and temperature on the erosion rates and mechanisms of modified EB PVD TBCs, *Wear*. 267 (2009) 1927–1934. doi:10.1016/j.wear.2009.04.002.
- [14] R.G. Wellman, M.J. Deakin, J.R. Nicholls, The effect of TBC morphology on the erosion rate of EB PVD TBCs, *Wear*. 258 (2005) 349–356. doi:10.1016/j.wear.2004.04.011.
- [15] R.G. Wellman, M.J. Deakin, J.R. Nicholls, The effect of TBC morphology and aging on the erosion rate of EB-PVD TBCs, *Tribology International*. 38 (2005) 798–804. doi:10.1016/j.triboint.2005.02.008.
- [16] S. Rezanka, D.E. Mack, G. Mauer, D. Sebold, O. Guillon, R. Vaßen, Investigation of the resistance of open-column-structured PS-PVD TBCs to erosive and high-temperature corrosive attack, *Surface and Coatings Technology*. 324 (2017) 222–235. doi:10.1016/j.surfcoat.2017.05.003.
- [17] D.E. Wolfe, M.P. Schmitt, D. Zhu, A.K. Rai, R. Bhattacharya, Multilayered Thermal Barrier Coating Architectures for High Temperature Applications, in: D. Zhu, H.-T. Lin, Y. Zhou, T. Hwang, M. Halbig, S. Mathur (Eds.), *Ceramic Engineering and Science Proceedings*, John Wiley & Sons, Inc., Hoboken, NJ, USA, 2012: pp. 1–18. <http://doi.wiley.com/10.1002/9781118217474.ch1> (accessed June 20, 2016).
- [18] R.J.L. Steenbakker, R.G. Wellman, J.R. Nicholls, Erosion of gadolinia doped EB-PVD TBCs, *Surface and Coatings Technology*. 201 (2006) 2140–2146. doi:10.1016/j.surfcoat.2006.03.022.
- [19] F. Cernuschi, L. Lorenzoni, S. Capelli, C. Guardamagna, M. Karger, R. Vaßen, K. von Niessen, N. Markocsan, J. Menuey, C. Giolli, Solid particle erosion of thermal spray and physical vapour deposition thermal barrier coatings, *Wear*. 271 (2011) 2909–2918. doi:10.1016/j.wear.2011.06.013.
- [20] F. Cernuschi, C. Guardamagna, S. Capelli, L. Lorenzoni, D.E. Mack, A. Moscatelli, Solid particle erosion of standard and advanced thermal barrier coatings, *Wear*. 348–349 (2016) 43–51. doi:10.1016/j.wear.2015.10.021.
- [21] M.P. Schmitt, A.K. Rai, D. Zhu, M.R. Dorfman, D.E. Wolfe, Thermal conductivity and erosion durability of composite two-phase air plasma sprayed thermal barrier coatings, *Surface and Coatings Technology*. 279 (2015) 44–52. doi:10.1016/j.surfcoat.2015.08.010.
- [22] M.P. Schmitt, B.J. Harder, D.E. Wolfe, Process-structure-property relations for the erosion durability of plasma spray-physical vapor deposition (PS-PVD) thermal barrier coatings, *Surface and Coatings Technology*. 297 (2016) 11–18. doi:10.1016/j.surfcoat.2016.04.029.
- [23] D. Shin, A. Hamed, Influence of micro-structure on erosion resistance of plasma sprayed 7YSZ thermal barrier coating under gas turbine operating conditions, *Wear*. 396–397 (2018) 34–47. doi:10.1016/j.wear.2017.11.005.
- [24] M.H. Vidal-Setif, N. Chellah, C. Rio, C. Sanchez, O. Lavigne, Calcium–magnesium–alumino-silicate (CMAS) degradation of EB-PVD thermal barrier coatings: Characterization of CMAS damage on ex-service high pressure blade TBCs, *Surface and Coatings Technology*. 208 (2012) 39–45. doi:10.1016/j.surfcoat.2012.07.074.

- [25] C.G. Levi, J.W. Hutchinson, M.-H. Vidal-Sétif, C.A. Johnson, Environmental degradation of thermal-barrier coatings by molten deposits, *MRS Bulletin*. 37 (2012) 932–941. doi:10.1557/mrs.2012.230.
- [26] R.G. Wellman, J.R. Nicholls, Erosion, corrosion and erosion–corrosion of EB PVD thermal barrier coatings, *Tribology International*. 41 (2008) 657–662. doi:10.1016/j.triboint.2007.10.004.
- [27] R. Naraparaju, M. Hüttermann, U. Schulz, P. Mechnich, Tailoring the EB-PVD columnar microstructure to mitigate the infiltration of CMAS in 7YSZ thermal barrier coatings, *Journal of the European Ceramic Society*. (2016). doi:10.1016/j.jeurceramsoc.2016.07.027.
- [28] A. Flores Renteria, A small-angle scattering analysis of the influence of manufacture and thermal induced morphological changes on the thermal conductivity of EB-PVD PYSZ thermal barrier coatings, 2007. http://darwin.bth.rwth-aachen.de/opus3/volltexte/2007/1790/pdf/Flores_Renteria_Arturo.pdf (accessed July 14, 2016).
- [29] R. Naraparaju, U. Schulz, P. Mechnich, P. Döbber, F. Seidel, Degradation study of 7wt.% yttria stabilised zirconia (7YSZ) thermal barrier coatings on aero-engine combustion chamber parts due to infiltration by different CaO–MgO–Al₂O₃–SiO₂ variants, *Surface and Coatings Technology*. 260 (2014) 73–81. doi:10.1016/j.surfcoat.2014.08.079.
- [30] R. Naraparaju, J.T. Gomez Chavez, U. Schulz, C.V. Ramana, Interaction and infiltration behavior of Eyjafjallajökull, Sakurajima volcanic ashes and a synthetic CMAS containing FeO with/in EB-PVD ZrO₂-65 wt% Y₂O₃ coating at high temperature, *Acta Materialia*. 136 (2017) 164–180. doi:10.1016/j.actamat.2017.06.055.
- [31] R.G. Wellman, J.R. Nicholls, On the effect of ageing on the erosion of EB-PVD TBCs, *Surface and Coatings Technology*. 177–178 (2004) 80–88. doi:10.1016/j.surfcoat.2003.06.019.
- [32] H. Berek, A. Yanina, C. Weigelt, C.G. Aneziris, Determination of the Phase Distribution in Sintered TRIP-Matrix / Mg-PSZ Composites using EBSD, *Steel Research Int*. 82 (2011) 1094–1100. doi:10.1002/srin.201100064.
- [33] R.G. Wellman, A. Dyer, J.R. Nicholls, Nano and Micro indentation studies of bulk zirconia and EB PVD TBCs, *Surface and Coatings Technology*. 176 (2004) 253–260. doi:10.1016/S0257-8972(03)00737-0.
- [34] J.R. Nicholls, Y. Jaslier, D.S. Rickerby, Erosion and Foreign Object Damage of Thermal Barrier Coatings, *Materials Science Forum*. 251–254 (1997) 935–948. doi:10.4028/www.scientific.net/MSF.251-254.935.
- [35] R.G. Wellman, J.R. Nicholls, Some observations on erosion mechanisms of EB PVD TBCs, *Wear*. 242 (2000) 89–96.
- [36] J. Eichler, U. Eisele, J. Rödel, Mechanical Properties of Monoclinic Zirconia, *Journal of the American Ceramic Society*. 87 (2004) 1401–1403. doi:10.1111/j.1151-2916.2004.tb07748.x.
- [37] C. Mercer, J.R. Williams, D.R. Clarke, A.G. Evans, On a ferroelastic mechanism governing the toughness of metastable tetragonal-prime (t') yttria-stabilized zirconia, *Proceedings of the Royal Society A: Mathematical, Physical and Engineering Sciences*. 463 (2007) 1393–1408. doi:10.1098/rspa.2007.1829.
- [38] F.F. Lange, Research of Microstructurally Developed Toughening Mechanisms in Ceramics. Parts 1-5., DTIC Document, 1980. <http://oai.dtic.mil/oai/oai?verb=getRecord&metadataPrefix=html&identifier=ADA098421> (accessed April 26, 2017).
- [39] A. Loganathan, A.S. Gandhi, Effect of phase transformations on the fracture toughness of t' yttria stabilized zirconia, *Materials Science and Engineering: A*. 556 (2012) 927–935. doi:10.1016/j.msea.2012.07.095.
- [40] V.L. Wiesner, N.P. Bansal, Mechanical and thermal properties of calcium–magnesium aluminosilicate (CMAS) glass, *Journal of the European Ceramic Society*. 35 (2015) 2907–2914. doi:10.1016/j.jeurceramsoc.2015.03.032.
- [41] G. Bolelli, L. Lusvardi, T. Manfredini, E. Parsini, C. Siligardi, BAS, CMAS and CZAS glass coatings deposited by plasma spraying, *Journal of the European Ceramic Society*. 27 (2007) 4575–4588. doi:10.1016/j.jeurceramsoc.2007.03.032.
- [42] T. Strangman, D. Raybould, A. Jameel, W. Baker, Damage mechanisms, life prediction, and development of EB-PVD thermal barrier coatings for turbine airfoils, *Surface and Coatings Technology*. 202 (2007) 658–664. doi:10.1016/j.surfcoat.2007.06.067.